

Neutron Transfer Dynamics and Doorway to Fusion in Time-Dependent Hartree-Fock Theory

A.S. Umar^{1a}, V.E. Oberacker¹, and J.A. Maruhn²

¹ Department of Physics and Astronomy, Vanderbilt University, Nashville, Tennessee 37235, USA

² Institut für Theoretische Physik, Goethe-Universität, 60438 Frankfurt am Main, Germany

Received: November 5, 2018/ Revised version: date

Abstract. We analyze the details of mass exchange in the vicinity of the Coulomb barrier for heavy-ion collisions involving neutron-rich nuclei using the time-dependent Hartree-Fock (TDHF) theory. We discuss the time-dependence of transfer and show that the potential barriers seen by individual single-particle states can be considerably different than the effective barrier for the two interacting nuclei having a single center-of-mass. For this reason we observe a substantial transfer probability even at energies below the effective barrier.

PACS. 21.60.Jz Nuclear Density Functional Theory and extensions – 24.10.Cn Many-body theory

1 Introduction

Heavy-ion fusion reactions are a sensitive probe of the size, shape, and structure of atomic nuclei as well as the collision dynamics. With the increasing availability of radioactive ion-beams the study of fusion reactions of neutron-rich nuclei are now possible [1, 2, 3]. Other experimental frontiers are the synthesis of superheavy nuclei in cold and hot fusion reactions [4, 6, 5, 7, 8], and weakly bound light systems [9, 10, 11, 12]. Microscopic descriptions of nuclear fusion may provide us with a better understanding of the interplay between the strong, Coulomb, and the weak interactions as well as the enhanced static and dynamic correlations present in these many-body systems.

Recently, two aspects of the collision dynamics leading to fusion that involve pre-compound neutrons have been of interest. Over the last decade a number of fusion studies have reported that the average number of neutrons evaporated by the compound nucleus is considerably less than what is predicted by statistical fusion evaporation calculations [13]. This phenomenon is quite possibly linked to the excitation of the pre-compound collective dipole mode, which is likely to occur when ions have significantly different N/Z ratio, and is a reflection of dynamical charge equilibration. This was studied in the context of TDHF in Refs. [14, 15, 16] and we have recently observed this phenomenon in the $^{64}\text{Ni}+^{132}\text{Sn}$ system [17]. Similarly, considerable attention has been given to the influence of neutron transfer on fusion cross-sections. Studies suggest that the transfer of neutrons with positive Q value strongly enhances the fusion cross-section in comparison to systems having negative Q value [18, 19, 20]. This may explain the

fact that lowering of the potential barrier for neutron-rich systems does not always lead to higher fusion cross-sections. In Ref. [19] near-barrier fusion of neutron-rich nuclei was studied within a channel coupling model for intermediate neutron rearrangement using a semi-empirical time-dependent three-body Schrödinger equation. Studies showed that for the $^{40}\text{Ca}+^{96}\text{Zr}$ system neutrons were transferred in the early stages of the collision from the $2d_{5/2}$ state of ^{96}Zr to the unoccupied levels of the ^{40}Ca nucleus.

It is generally acknowledged that the TDHF method provides a useful foundation for a fully microscopic many-body theory of low-energy heavy-ion reactions [21]. Historically, fusion in TDHF has been viewed as a final product of two colliding heavy-ions, and the dynamical details influencing the formation of the compound system have not been carefully dissected in terms of the pre-compound properties. Due to the availability of much richer fusion data and considerable advances in TDHF codes that make no symmetry assumptions and use better effective interactions, it may now be possible to examine these effects more carefully. In TDHF complete fusion proceeds by converting the entire relative kinetic energy in the entrance channel into internal excitations of a single well-defined compound nucleus. The dissipation of the relative kinetic energy into internal excitations is due to the collisions of the nucleons with the “walls” of the self-consistent mean-field potential. TDHF studies demonstrate that the randomization of the single-particle motion occurs through repeated exchange of nucleons from one nucleus into the other. Consequently, the equilibration of excitations is very slow, and it is sensitive to the details of the evolution of the shape of the composite system. This is in contrast to most classical

^a *e-mail:* umar@compsci.cas.vanderbilt.edu

pictures of nuclear fusion, which generally assume near instantaneous, isotropic equilibration. The relaxation of the final compound system is a long-time process occurring on a time scale on the order of a few thousand fm/c . In contrast, the pre-compound stage corresponds to a time scale of a few hundred fm/c .

In this manuscript we focus on the analysis of transfer during the early stages of the collision. In particular, we confirm the findings of Ref. [19]. We also show that in TDHF different single-particle states seem to see different potential barriers in comparison to the generic ion-ion barrier. This influences the overall dynamics leading to fusion and consequently the effective potential barrier.

2 Transfer in TDHF

The TDHF calculations have been carried out using our new three-dimensional unrestricted TDHF code [22]. For the effective interaction we have used the Skyrme SLy4 force [23], including all of the time-odd terms. Static Hartree-Fock calculations for all the nuclei studied here produce spherically symmetric systems. The chosen mesh spacing was 1 fm in all three directions, which yield a binding energy accuracy of about 50 keV in comparison to a spherical Hartree-Fock code. For these calculations we have in addition required that the fluctuations in energy be as low as 10^{-4} - 10^{-5} , the corresponding accuracy in binding energy is about 10^{-12} . This ensures that the tails of the wavefunctions are well converged in the numerical box. The box size used was 60 fm in the direction of the collision axis and 30 fm in the other two directions. The initial nuclear separations were 25 fm.

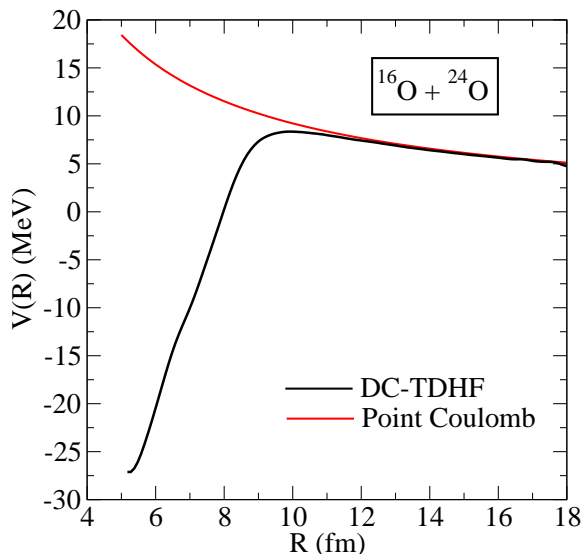


Fig. 1. Potential barrier, $V(R)$, for the $^{16}\text{O}+^{24}\text{O}$ system obtained from density constrained TDHF calculations (black curve). Also shown is the point Coulomb potential (red curve).

2.1 $^{16}\text{O}+^{24}\text{O}$ system

As an example of a collision involving one neutron rich nucleus we studied the $^{16}\text{O}+^{24}\text{O}$ system. In order to determine the potential barrier for the system we have used the DC-TDHF method as described in Ref. [24]. In this approach the TDHF time-evolution takes place with no restrictions. At certain times during the evolution the instantaneous density is used to perform a static Hartree-Fock minimization while holding the neutron and proton densities constrained to be the corresponding instantaneous TDHF densities. Some of the effects naturally included in the DC-TDHF calculations are: neck formation, particle exchange, internal excitations, and deformation effects to all order. The heavy-ion potential was obtained by initializing the system at $E_{c.m.} = 9.5$ MeV, which is slightly above the barrier shown in Fig. 1. The peak of the barrier is about 8.4 MeV at a nuclear separation of 9.9 fm. This is lower than the barrier of the $^{16}\text{O}+^{16}\text{O}$ system, which has a height of about 10 MeV. Here and in the following, the heavy-ion interaction potential has been calculated with a constant mass parameter corresponding to the reduced mass of the ions. This is a good approximation as long as one is only interested in the value of the potential barrier height (as is the case here). For the calculation of sub-barrier fusion cross sections, however, it is essential that coordinate-dependent mass parameters be utilized [17] because the cross sections depend sensitively on the shape of the potential in the interior region.

In order to examine the center-of-mass energy dependence of mass exchange below and above the barrier we have initiated TDHF collisions at energies $E_{c.m.} = 6, 7, 8, 9,$ and 9.5 MeV. Interestingly, the head-on (zero impact parameter) TDHF collisions for the lowest four energies behave as a typical sub-barrier collision: the two ions approach a minimum distance with no visible overlap, then recoil and move away from each other. This is also true for $E_{c.m.} = 9$ MeV despite the fact that this energy lies above the ion-ion barrier. This suggests that while we can talk about an *effective* ion-ion barrier the individual single-particle states may see a barrier somewhat different than the effective one. This is in agreement with the findings of Ref. [19], and we shall come back to this point again later in the manuscript. Even though we are dealing with sub-barrier energies, we observe mass exchange (mainly neutron) from ^{24}O to ^{16}O for all these energies. Similarly, we observe a small dissipation of the relative kinetic energy, ranging from 0.05 MeV for $E_{c.m.} = 6$ MeV to 0.40 MeV for $E_{c.m.} = 9$ MeV. For comparison, the difference in total energy of the system before and after the collision is on the order of 0.02 MeV, i.e., the numerical error in total energy conservation is less than the dissipated energy, even at very low energies. At $E_{c.m.} = 9.5$ MeV the system fuses.

To gain further insight into the mass exchange we have looked at the change in nuclear density along the collision axis (z -axis). We define

$$\rho(z, t) = \int dx \int dy \rho(x, y, z, t), \quad (1)$$

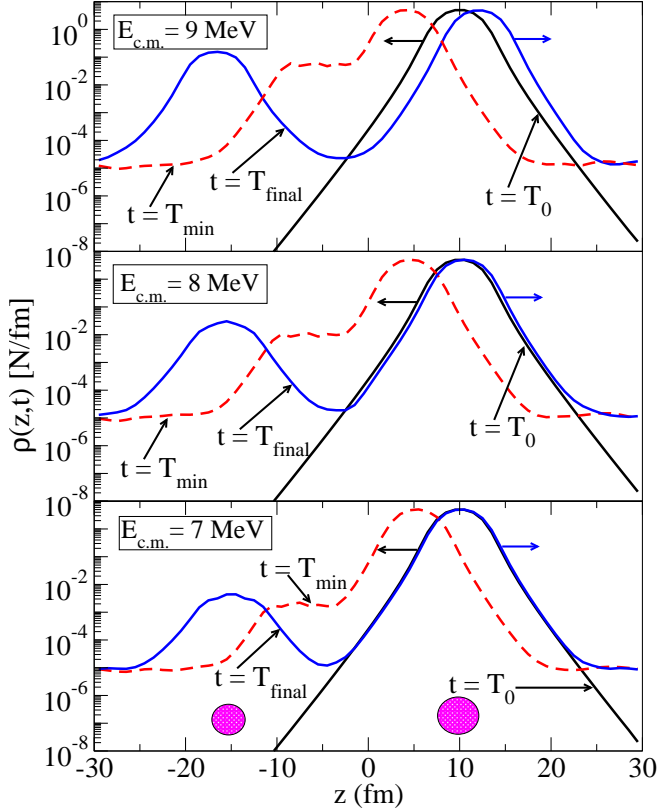


Fig. 2. Partially integrated neutron densities calculated from Eq.(1) for the ^{24}O nucleus plotted on a logarithmic scale versus the collision axis coordinate z for the $^{16}\text{O}+^{24}\text{O}$ system at three energies, $E_{c.m.} = 7, 8,$ and 9 MeV. The black-solid curves correspond to the initial partial density, the red-dashed curves are the same quantity at the distance of closest approach, and the blue-solid curves are partial densities long after the recoil. Filled spheres near the bottom axis approximately show the initial and final location of the two nuclei.

where $\rho(x, y, z, t)$ is the instantaneous TDHF density. In Fig. 2 we plot $\rho(z, t)$ for three energies, $E_{c.m.} = 7, 8,$ and 9 MeV, on a logarithmic scale versus the collision axis coordinate z . We emphasize that the plotted density contains only states that correspond to the ^{24}O nucleus. The black-solid curves correspond to the initial partial density, the red-dashed curves are the same quantity at the distant of closest approach, and the blue-solid curves are partial densities long after the recoil. Filled spheres near the bottom axis denote the approximate initial and final location of the two nuclei. The distance of closest approach for energies $E_{c.m.} = 7, 8,$ and 9 MeV are 13.2 fm, 11.6 fm, and 10.1 fm, respectively. Two features are worth noting: first, we see a buildup of the density on the ^{16}O side of the reaction plane, and secondly, we note that the buildup gets substantially larger with increasing energy. We also observe that the recoiled density profile remains very close to the initial profile except in the tail region. The corresponding mass transfer ΔA at sub-barrier energies can be found by integrating $\rho(z, t)$ over the z values on the left side of the minimum. At energies $E_{c.m.} = 7, 8,$ and 9 MeV we find mass transfer values of $0.024, 0.1464,$ and

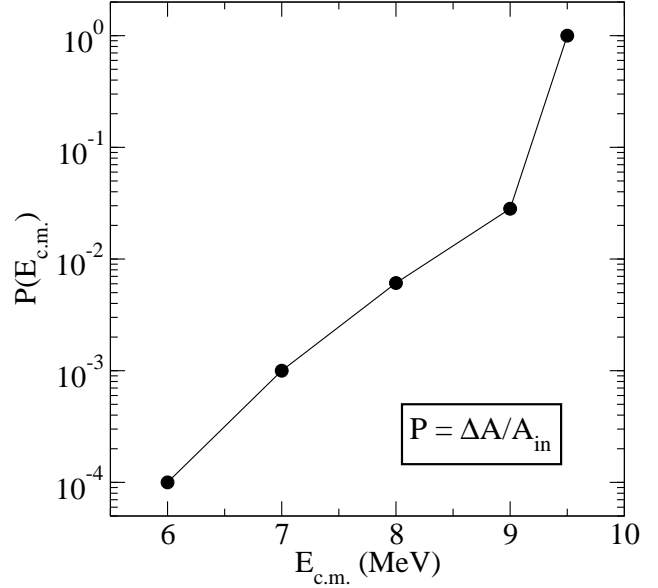


Fig. 3. Mass transfer probability defined in Eq. (2) for the transfer in the $^{16}\text{O}+^{24}\text{O}$ system.

$0.6768,$ respectively. The mass transfer at $E_{c.m.} = 6$ MeV is 0.0022 . We emphasize that unitarity (or total mass number) was conserved with an accuracy of about one part in 10^5 . In Fig. 3 we plot the energy dependence of the transfer probability defined as

$$P(E_{c.m.}) = \frac{\Delta A(E_{c.m.})}{A_{in}}, \quad (2)$$

where ΔA is the mass exchange value mentioned above and A_{in} is the mass of the incoming nucleus, in this case 24 . We observe that for sub-barrier energies the curve is essentially linear and jumps to one when fusion occurs.

In order to identify which of the single-particle states are predominantly responsible for transfer at sub-barrier energies we define the quantity

$$P_\alpha(z, t) = \int dx \int dy |\psi_\alpha(x, y, z, t)|^2, \quad (3)$$

where the ψ_α 's are single-particle states. In Fig. 4 we plot this quantity on a logarithmic scale for the neutron states of the ^{24}O nucleus at $E_{c.m.} = 7$ MeV, long after the recoil, at which time the ion-ion separation is about $R = 25$ fm. Although our single-particle wave functions are calculated on a 3-D Cartesian grid and thus do not carry the same good quantum numbers as the spherical representation, for a well converged spherical nucleus it is possible to calculate the expectation values of orbital angular momentum, spin, and parity to identify these states. As expected, the contribution to the sub-barrier mass transfer is primarily coming from the $2s_{1/2}$ neutron state of the ^{24}O nucleus. The contribution from the $d_{5/2}$ and $d_{3/2}$ states is an order of magnitude lower than that of the $2s_{1/2}$ state. This again suggests that the barrier seen by the $2s_{1/2}$ state is different than the effective barrier for the entire nucleus.

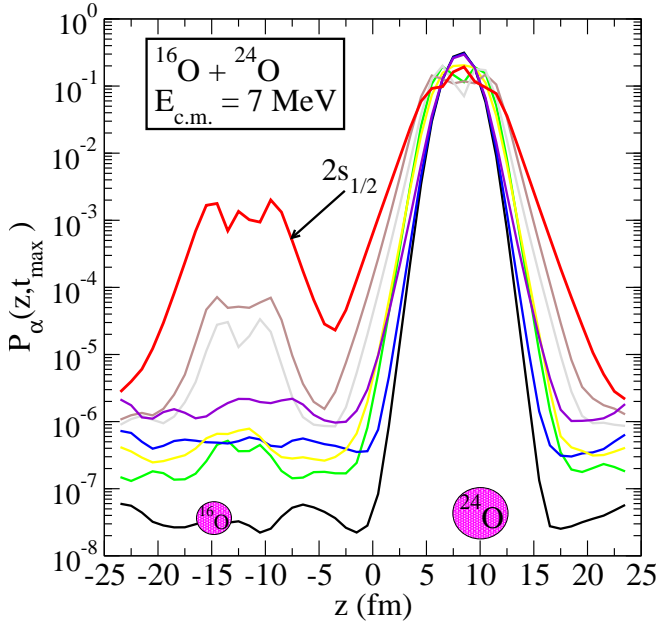


Fig. 4. Neutron single-particle probability densities given by Eq. (3) for the ^{24}O nucleus at $E_{\text{c.m.}} = 7$ MeV at $t = T_{\text{final}}$. Filled spheres near the bottom axis approximately show the final location of the two nuclei.

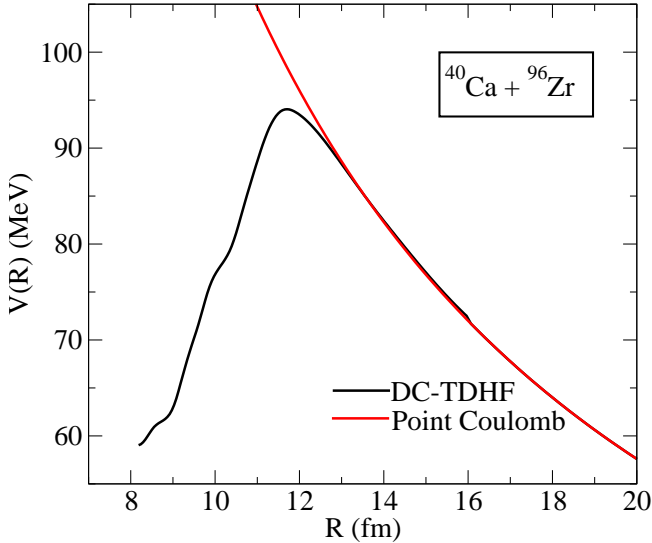


Fig. 5. Potential barrier, $V(R)$, for the $^{40}\text{Ca} + ^{96}\text{Zr}$ system obtained from density constrained TDHF calculations (black curve). Also shown is the point Coulomb potential (red curve).

2.2 $^{40}\text{Ca} + ^{96}\text{Zr}$ system

In Ref. [19] fusion for neutron-rich systems was studied in the vicinity of the Coulomb barrier using a semi-empirical time-dependent three-body Schrödinger equation. Their studies showed that for the $^{40}\text{Ca} + ^{96}\text{Zr}$ system at $E_{\text{c.m.}} = 97$ MeV, which is in the vicinity of the Coulomb barrier, neutrons were transferred in the early stages of the collision ($R = 11\text{--}14$ fm) from the $2d_{5/2}$ state of ^{96}Zr to the unoccupied levels of the ^{40}Ca nucleus. Here, we shall study the same system using the TDHF theory. We have used the

DC-TDHF method to find the effective potential barrier for this system as shown in Fig. 5. The barrier was calculated by initializing the TDHF run at $E_{\text{c.m.}} = 97$ MeV. The barrier peak is about 95 MeV and is located at about $R = 11.5$ fm. For this energy the TDHF collision results in fusion. In order to establish the early mass exchange we have plotted the nuclear density and the corresponding neutron density of the ^{96}Zr nucleus (which is on the right half of the collision plane) in Fig. 6. The neutron density was plotted on a logarithmic scale to emphasize the low-density contours. The neutron tail seen in the lower frame of Fig. 6 is very similar to the neutron density contours shown in Fig. 10 of Ref. [19]. For the same energy we have

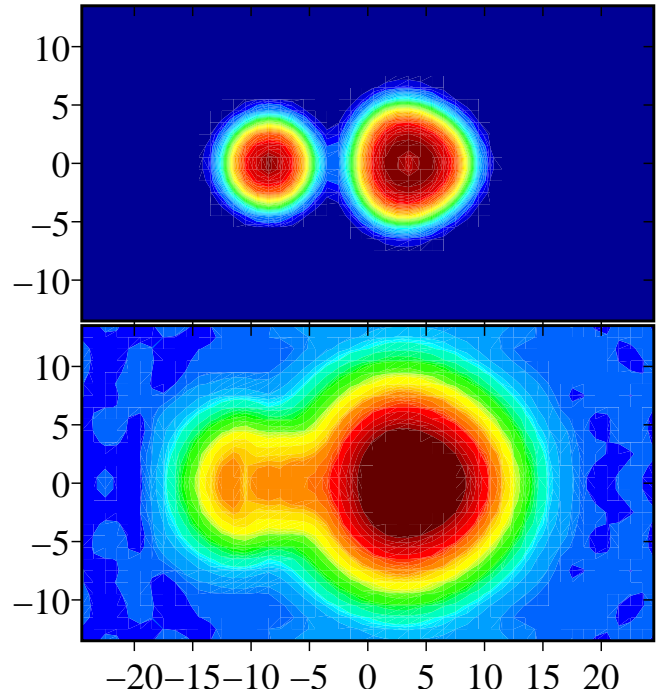


Fig. 6. Contours of the total density for the dinuclear system $^{40}\text{Ca} + ^{96}\text{Zr}$ at ion-ion separation of $R = 12.3$ fm (top frame), and contours of the ^{96}Zr neutron states, plotted on a logarithmic scale at the same separation (bottom frame).

also calculated the partially integrated neutron density as a function of the collision axis coordinate z using Eq.(1) for the ^{96}Zr nucleus, shown in Fig. 7. In this case we do not have a recoiled final state since the system actually fuses. The integrated neutron transfer at the ion-ion separation distance of about $R = 12$ fm is approximately 0.5.

To identify which states actually contribute to the probability of mass exchange from ^{96}Zr to ^{40}Ca we have plotted the individual neutron single-particle probabilities given by Eq. (3) for the ^{96}Zr nucleus as a function of collision coordinate axis z at the same ion-ion separation $R = 12.3$ fm, as shown in Fig. 8. Again, the static Hartree-Fock calculation for the ^{96}Zr nucleus helps us identify these states. The states up to $N = 50$ can be enumerated (by using parity, degeneracy of eigenvalues, etc.) and

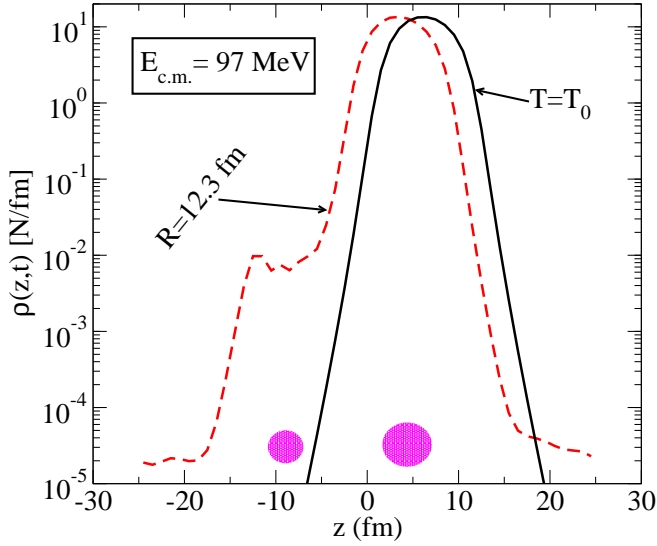


Fig. 7. Partially integrated neutron density calculated from Eq.(1) for the ^{96}Zr nucleus plotted on a logarithmic scale versus the collision axis coordinate z for the $^{40}\text{Ca}+^{96}\text{Zr}$ system at $E_{\text{c.m.}} = 97$ MeV. The solid black curve corresponds to the initial partial density and the dashed red curve to the same quantity at $R = 12.3$ fm.

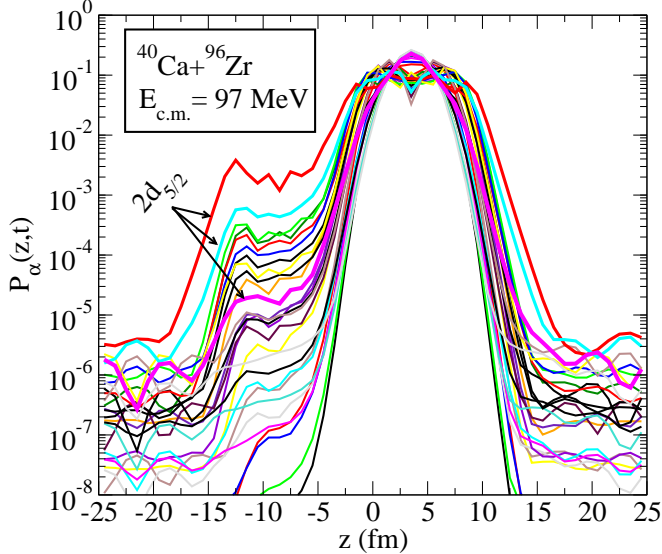


Fig. 8. Neutron single-particle probability densities given by Eq. (3) for the ^{96}Zr nucleus at $E_{\text{c.m.}} = 97$ MeV at $R = 12.3$ fm.

exactly match the shell-model states with the spin-orbit term. The last six states (we do not impose time-reversal invariance and thus have one state per nucleon) are almost degenerate in energy and have positive parity values. This is consistent with Ref. [19], which finds the neutron to be in the $2d_{5/2}$ state. The corresponding three states (time-reversed pairs) are the red, cyan, and magenta colored curves drawn thicker than others and pointed out by arrows. We observe that while two of the states are the largest contributors to the transmission probability, one of the states practically makes no contribution. This is true

despite the fact that all these states are the highest energy states and are degenerate in energy. After the second highest $2d_{5/2}$ state at -7.05 MeV (cyan) the next three states that have the largest contribution to the transmission probability are; one of the two $2p_{3/2}$ states at -18.06 MeV, the $2p_{1/2}$ state at -16.17 MeV, and only one of the five $1g_{9/2}$ states at -12.26 MeV. The single-particle quadrupole moment is a good indicator of which of the states, specially sub-states belonging to the same quantum number, make the largest contribution to the transmission probability, since the most stretched states have the largest positive quadrupole moments. For example the three sub-states of the $2d_{5/2}$ state have single-particle quadrupole moments of 11.8 , 3.7 , and -15.6 fm^2 corresponding to the three states shown in Fig. 8 in descending order. Similarly, the $2p_{3/2}$ state with a quadrupole moment of 8.0 fm^2 is the next largest contributor whereas the other sub-state with a quadrupole moment of -8.0 fm^2 has a transmission probability which is orders of magnitude smaller. It

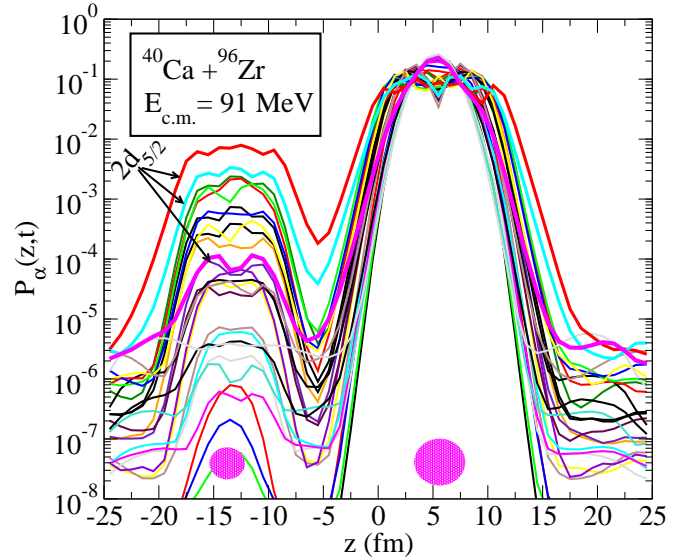


Fig. 9. Neutron single-particle probability densities given by Eq. (3) for the ^{96}Zr nucleus at $E_{\text{c.m.}} = 91$ MeV and after the recoiling nuclei are at a separation of $R = 19$ fm.

is interesting to note that some of the sub-states of the same quantum number give a much larger contribution, and states like $1f_{5/2}$, which is higher in energy than $2p_{3/2}$, do not contribute appreciably. This seems to indicate that the transmission probability depends not only on the energies of the single-particle states, but that it has an additional strong dependence on other properties of the states. We have also repeated the same study for the $^{40}\text{Ca}+^{96}\text{Zr}$ system at $E_{\text{c.m.}} = 91$ MeV, which is below the effective barrier. In this case the nuclei recoil with a closest approach distance of 12.6 fm. Again, in order to identify which states actually contribute to the probability of mass exchange from ^{96}Zr to ^{40}Ca we have plotted the individual neutron single-particle probabilities given by Eq. (3) for the ^{96}Zr nucleus as a function of collision coordinate axis

z when the recoiled ions are about $R = 19$ fm apart, as shown in Fig. 9. We observe that the single-particle transmission probabilities after the recoiled nuclei are well separated are similar to the findings for the $E_{c.m.} = 97$ MeV case, except with reduced probabilities. In addition, the observed sub-barrier behavior for the $^{40}\text{Ca}+^{96}\text{Zr}$ system is analogous to the $^{16}\text{O}+^{24}\text{O}$ system.

3 Conclusions

We have performed a detailed analysis of mass exchange in the vicinity of the Coulomb barrier for systems involving a neutron-rich nucleus using the TDHF theory. Our work was motivated by Ref. [19] where the same phenomenon was studied using a quantum mechanical three-body model. For the $^{40}\text{Ca}+^{96}\text{Zr}$ system at $E_{c.m.} = 97$ MeV, which is slightly above the barrier, we can essentially confirm the results of Ref. [19]. We confirm that at relatively large ion-ion distances the neutron transfer probability begins to build up at the location of the receiving nucleus. We have analyzed this aspect of neutron transmission in TDHF using the lighter $^{16}\text{O}+^{24}\text{O}$ system. We find that in the vicinity of the Coulomb barrier and below the barrier different single-particle states see barriers that may differ from the effective ion-ion barrier with a fixed center-of-mass. This reflects the fact that the single-particle wave functions feel the barrier in the mean field potential between the two nuclei, both concerning its height and its position relative to their own geometric distribution, while the ion-ion barrier is a bulk effect. Due to this fact we find appreciable transfer probability for energies well below the effective barrier. This confirms that the incorporation of neutron transfer effects, as well as other effects which depend on the properties of the single-particle states, are necessary ingredients in fusion barrier calculations.

This work has been supported by the U.S. Department of Energy under grant No. DE-FG02-96ER40963 with Vanderbilt University, and by the German BMBF under contract No. 06 F 131.

References

1. J. F. Liang *et al.*, Phys. Rev. Lett. **91**, 152701 (2003); Phys. Rev. Lett. **96**, 029903(E) (2006).
2. J. F. Liang and C. Signorini, Int. J. Mod. Phys. E **14**, 1121 (2005).
3. C. L. Jiang *et al.*, Phys. Rev. Lett. **93**, 012701 (2004).
4. S. Hofmann *et al.*, Eur. Phys. J. **A14**, 147 (2002).
5. T. N. Ginter *et al.*, Phys. Rev. C **67**, 064609 (2003).
6. Yu. Ts. Oganessian *et al.*, Phys. Rev. C **69**, 021601(R) (2004).
7. K. Morita *et al.*, Eur. Phys. J. **A21**, 257 (2004).
8. T. Ichikawa, A. Iwamoto, P. Möller, and A.J. Sierk, Phys. Rev. C **71**, 044608 (2005).
9. Yu. E. Penionzhkevich, V. I. Zagrebaev, S. M. Lukyanov, and R. Kalpakchieva, Phys. Rev. Lett. **96**, 162701 (2006).
10. A. Di Pietro, *et al.*, Phys. Rev. C **69**, 044613 (2004).
11. J. J. Kolata, *et al.*, Phys. Rev. Lett. **81**, 4580 (1998).
12. M. Trotta, *et al.*, Phys. Rev. Lett. **84**, 2342 (2000).
13. O. Wieland, *et al.*, Phys. Rev. Lett. **97**, 012501 (2006)
14. C. Simenel, Ph. Chomaz, and G. de France, Phys. Rev. Lett. **86**, 2971 (2001).
15. C. Simenel, Ph. Chomaz, and G. de France, Phys. Rev. C **76**, 024609 (2007).
16. A. S. Umar, M. R. Strayer, R. Y. Cusson, P. -G. Reinhard, and D. A. Bromley, Phys. Rev. C **32**, 172 (1985).
17. A. S. Umar and V. E. Oberacker, Phys. Rev. C **76**, 014614 (2007).
18. J. F. Liang *et al.*, Phys. Rev. C **75**, 054607 (2007).
19. V. I. Zagrebaev, V. V. Samarin, and W. Greiner, Phys. Rev. C **75**, 035809 (2007).
20. C.H. Dasso, S. Landowne, and A. Winther, Nucl. Phys. **A407**, 221 (1983).
21. J. W. Negele, Rev. Mod. Phys. **54**, 913 (1982).
22. A. S. Umar and V. E. Oberacker, Phys. Rev. C **73**, 054607 (2006).
23. E. Chabanat, P. Bonche, P. Haensel, J. Meyer and R. Schaeffer, Nucl. Phys. **A635**, 231 (1998); Nucl. Phys. **A643**, 441(E) (1998).
24. A. S. Umar and V. E. Oberacker, Phys. Rev. C **74**, 021601(R) (2006).